applied sciences

MDPI

*Article*

# Non-Destructive Multi-Method Assessment of Steel Fiber Orientation in Concrete †

**Sabine Kruschwitz [1,2,*], Tyler Oesch [1,‡,3], Frank Mielentz [1], Dietmar Meinel [1] and Panagiotis Spyridis [4]**

[1] Bundesanstalt für Materialforschung und -prüfung (BAM), 12205 Berlin, Germany; frank.mielentz@bam.de (F.M.); dietmar.meinel@bam.de (D.M.)
[2] Institute of Civil Engineering, Technische Universität Berlin, 13355 Berlin, Germany
[3] Federal Office for the Safety of Nuclear Waste Management (BASE), 11513 Berlin, Germany; tyler.oesch@bfe.bund.de (T.O.)
[4] Faculty of Architecture and Civil Engineering South Campus, Technische Universität Dortmund, 44227 Dortmund, Germany; panagiotis.spyridis@tu-dortmund.de (P.S.)
* Correspondence: sabine.kruschwitz@bam.de; Tel.: +49-30-8104-1442 (S.K.)
† This paper is an extended version of paper published in the 17th fib Symposium, Concrete Structures for Resilient Society held in Shanghai, China, 22–24 November 2020 online. ISSN: 2617-4820, ISBN: 978-2-940643-04-2.
‡ Denotes a former employer.

**Abstract:** Integration of fiber reinforcement in high-performance cementitious materials has become widely applied in many fields of construction. One of the most investigated advantages of steel fiber reinforced concrete (SFRC) is the deceleration of crack growth and hence its improved sustainability. Additional benefits are associated with its structural properties, as fibers can significantly increase the ductility and the tensile strength of concrete. In some applications it is even possible to entirely replace the conventional reinforcement, leading to significant logistical and environmental benefits. Fiber reinforcement can, however, have critical disadvantages and even hinder the performance of concrete, since it can induce an anisotropic material behavior of the mixture if the fibers are not appropriately oriented. For a safe use of SFRC in the future, reliable non-destructive testing (NDT) methods need to be identified to assess the fibers' orientation in hardened concrete. In this study, ultrasonic material testing, electrical impedance testing, and X-ray computed tomography have been investigated for this purpose using specially produced samples with biased or random fiber orientations. We demonstrate the capabilities of each of these NDT techniques for fiber orientation measurements and draw conclusions based on these results about the most promising areas for future research and development.

**Keywords:** steel fiber reinforced concrete; fiber orientation; non-destructive testing; micro-computed tomography; ultrasound; spectral induced polarization

check for updates

**Citation:** Kruschwitz, S.; Oesch, T.; Mielentz, F.; Meinel, D.; Spyridis, P. Non-Destructive Multi-Method Assessment of Steel Fiber Orientation in Concrete. *Appl. Sci.* **2022**, *12*, 697. https://doi.org/10.3390/app12020697

Academic Editors: Dario De Domenico, Jerzy Hoła and Łukasz Sadowski

Received: 29 November 2021
Accepted: 5 January 2022
Published: 11 January 2022



## 1. Introduction

In recent decades, the addition of short fibers in modern structural concrete has been a preferred option for improving the composite material's performance under tensile stress states. In relation to plain concrete, steel fiber-reinforced concrete (SFRC) shows not only higher resistance to crack growth, and hence improved resistance to aggressive substance diffusion and increased durability [1], but also enhanced tensile strength and ductility. Frequent industrial applications of SFRC include high-performance slabs (such as industrial floors, pile-supported foundation rafts and slabs on grade), tunnel linings, refractory structures, silos, containers, impact-proof defence structures and prefabricated—often prestressed—structural components. Because of the increasing trend for the use of SFRC in several types of engineering structures, advanced knowledge and standardisation with respect to this material becomes essential. The increasing interest in design guidance for SFRC is reflected in, besides numerous scientific publications and dedicated conferences,

the emerging guidelines and standards, e.g., in the fib Model Code 2010 and 2020 [2,3], the German standard DIN 1045 and the associated DAfStb-Richtlinie Stahlfaserbeton [4], the ACI 544.4 Guide to Design with Fiber-Reinforced Concrete [5] and, most importantly, in the inclusion of provisions for the design with SFRC in the next generation of Eurocode 2 [6]. The design with SFRC strongly depends on the properties of the fiber reinforcement, such as the dosage of the fibers (typically expressed in weight of fibers per total volume of concrete), the material (steel, natural, synthetic), the dimensions (length and cross-section) and the shape of the fibers (straight, crimped, hooked, etc.) Furthermore, modern design concepts strongly rely on consistent and predictable overall distribution and orientation characteristics for fibers in the hardened concrete mix, since the amount and inclination of the fibers relative to the internal stress directions of the structural component have been shown to significantly influence its load-bearing performance [7]. Alignment of fibers in a parallel direction to the prevailing tensile stresses understandably increases the composite matrix's resistance in tensile rupture, and unfavorable fiber distributions and orientations can even hinder the structural performance of concrete by inducing anisotropy and weak regions in the material.

Fiber reinforcement in concrete aims to mainly arrest the concrete crack formation and propagation, which generally results in an increased tensile strength, ductility, and durability of the material. As seen in Figure 1, this effect is strongly dependent on the location of the fibers within the concrete matrix with respect to the cracking, which in turn forms in a nearly perpendicular direction to the tensile stresses in the material. These stresses are in turn bridged through the fibers intersecting the crack. Obviously, this behavior is strongly influenced by the orientation of fibers in relation to the principal tensile stresses (represented by the black arrows) and the resulting cracking planes. The fibers can, for example, have an orientation parallel to the cracking plane (blue), they can have a random orientation distribution in relation to the stress and crack planes (yellow), or be aligned parallel to the tensile forces and perpendicularly to the crack plane (red). In the last case (red), an optimum utilisation of the fibers' cross section is expected, and hence the load-displacement response can exhibit substantial ductility and possibly higher strength than plain concrete, which would otherwise fail in a quasi-brittle manner after the crack initiation. The yellow fibers represent the random distribution, which can still exhibit cracking stress retention and, hence, ductility. In the most suboptimal (blue) case, fibers essentially do not contribute to crack bridging, and, hence, concrete tends to behave similarly to a plain unreinforced material. In fact, fibers in this latter orientation can even act as discontinuities in the matrix and accelerate cracking. The fiber distribution and orientation strongly depends on the casting conditions of the fresh mix as well as geometric constraints, and the effect of casting-induced variations in fiber orientations on SFRC structural performance has been shown in previous research [8–11]. Some methods to control the fiber alignment in fresh concrete have also been proposed, e.g., by [12,13]. The effect of the fiber orientations on the load-bearing performance of concrete is accounted for in current design guidelines [2,14] by introducing a so-called fiber orientation factor, which reduces the nominal tensile strength value of fiber reinforced concrete, accounting for favorable and unfavorable fiber alignment effects as well as isotropy.

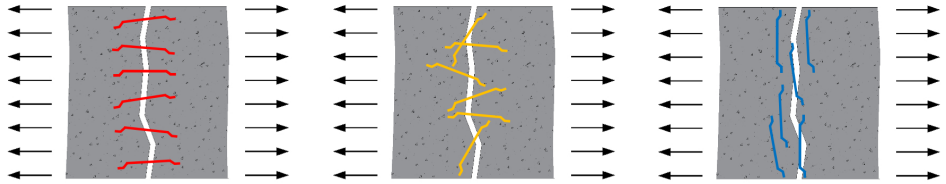

**Figure 1.** Indicative alignment of fibers in relation to tensile stresses and cracking in concrete, from left to right: most favorable, with fibers (red) aligned with the tensile stresses; random (yellow), leading to isotropic performance; and unfavorable (blue) with no fibers (effectively) bridging the crack.

Given the critical effect that fiber orientation and distribution have on the strength and failure pattern of SFRC structural components, NDT methods for evaluating fiber orientation and distribution are needed. In addition to measurement systems that can be applied in the lab on small samples, e.g., in [15], in situ testing techniques for large structures need to be developed.

In this study, we focus on the application of methods, which have already shown some value in this regard but have not yet really been systematically applied on samples with defined amounts of fibers in different orientations.

Previous research has indicated that electrical resistivity could be a suitable tool for the measurement of fiber orientations [16] and fiber-volume fractions in larger SFRC structural components [17,18]. Dry cementitious materials are typically electrical insulators. However, conducting materials added to the concrete, such as steel fibers, significantly decrease its electrical resistivity. Nontheless, further research is still needed in order to precisely define quantitative values of steel fiber distribution and orientation based on electrical resistivity data. The frequency dependency of the electrical resistivity and, hence, the polarizability of SFRC in the low frequency range has not yet been studied. It is conceivable that looking at both the capability of a medium to conduct and to store electrical charges will give deeper insight for material characterization. This can, for example, be done when the spectral induced polarization (SIP) method is used for measuring the electrical properties of a medium.

Recent research has also indicated that ultrasonic techniques may be useful for assessing fiber orientation characteristics [19]. If such an ultrasonic-based method could be validated, it would hold great potential, since ultrasound measurement techniques are already widespread within the civil engineering community and the capability of measuring ultrasonic properties up to several meters in depth has been successfully demonstrated [20]. However, further research is still needed to determine the sensitivity and accuracy of ultrasound for fiber orientation measurement, including ultrasound measurement quality and consistency for varying fiber types, structural shapes, and concrete mixtures.

One of the most popular NDT methods for measuring the spatial distribution and directional orientation of fibers in concrete in the lab is X-ray computed tomography (CT) [21–23]. When used for analysis of SFRC, this method typically relies on the fact that the fibers have significantly higher X-ray attenuations than the surrounding concrete material. The primary drawbacks of this method are, however, that specimen sizes tend to be limited and that X-ray CT cannot easily be used on-site in actual structures. Regardless, the accuracy of fiber measurement using X-ray CT on small specimens makes it an ideal method for calibrating or validating fiber measurements using other NDT techniques.

The study described in this paper was undertaken in order to assess the general sensitivity of the ultrasonic and SIP methods for fiber orientation measurement and to identify promising areas for future research. To accomplish these goals, specimens with varying controlled, casting-induced fiber orientation characteristics were fabricated and subsequently measured using ultrasonic and SIP measurement systems. Following these measurements, the specimens were scanned using X-ray CT and fiber orientation analyses of the resulting CT images were carried out. The goal of these CT-based analyses was to provide precise fiber orientation data for validation of the results of the ultrasonic and SIP measurements.

## 2. Materials and Methods

### 2.1. Sample Material

In the framework of the investigations presented herein, five samples with varying fiber alignments were produced and tested. For the sample examinations, it was required to create samples with randomly distributed fibers, and with fibers aligned parallel and transversely to the sample main axis. Depending on the test type and configuration, different sample dimensions were required: the samples used for ultrasound testing were prismatic with dimensions of 80 × 80 × 300 mm, while the SIP- and CT-based evaluations used

smaller cylindrical samples with a diameter of 50 mm and a length of 150 mm. The prismatic samples were initially cast as described below. Following ultrasonic measurement, the cylindrical samples were extracted from these prisms through diamond core drilling along their longitudinal axis.

The material used was identical for all samples: a concrete of class C35/45 having a target mean compressive strength of 50 MPa. The mix included CEM I 42.5 R cement from the producer Phoenix Zementwerke Krogbeumker Holding GmbH & Co. KG at 344 kg/m$^3$, added water at 147 kg/m$^3$ (w/c = 0.43), aggregates from the Rhine river plant of Hülskens GmbH & Co. KG with grading of 0/2, 2/8 and 8/16 mm at 779, 574, and 571 kg/m$^3$ (or 40%, 30%, and 30%), respectively, and no further admixtures. Furthermore, hooked-ended 5D Dramix® fibers 5D 65/60 BG (with 62 mm length and 0.9 mm diameter ([24]) and fy = 2300 N/mm$^2$) were used. Fiber dosages of 80 kg/m$^3$ (or 1 vol.%) and 40 kg/m$^3$ (or 0.5 vol.%) were realised in the samples (Figure 2, right). One sample was cast without any fibers for reference. The air void content in all samples was estimated as ca. 1.5% per mix volume.


**Figure 2.** Photograph of steel fibers Dramix 5D (**left**) and photograph during the sequential concrete and fiber laying for orthotropic samples at the laboratory of the TU Dortmund (**right**).

In order to produce the samples, the concrete material was mechanically mixed in a small laboratory concreting barrel without fibers. A portion was separated and kept without fibers, then fibers were added in the rest of the mix and it was further mixed in order to obtain a homogeneous spatial and orientational distribution of the fibers. This latter material was then directly cast in prismatic moulds. In order to produce the samples with orthotropically aligned fibers, the withheld plain concrete portion was cast sequentially in layers, followed by a manual placement of the fibers in the desired alignment (Figure 2, right). At intervals, the samples were compacted on a vibrating plate.

A photo of all prepared samples is shown in Figure 3. However, in this paper, we will investigate and explain in detail the potential of the NDT methods using five selected specimens as examples. These are three specimens with 40 kg/m$^3$ fiber content, where the fibers are distributed longitudinally, transversely as well as randomly. Furthermore, the results of a sample with 80 kg/m$^3$ fibers arranged longitudinally to the sample axis and a sample without fibers are discussed. The samples with random fiber distribution, and with fibers aligned parallel and transversely to the longitudinal sample axis are denoted throughout the paper using the specifications *, | | |, and —, respectively. The fiber dosage is stated in the sample name as either 40 or 80 according to their amount of fibers in kg/m$^3$. The specimen preparation was performed in the concreting facilities of the Building Research Lab at the TU Dortmund. All samples discussed in the following are colour coded in Figure 3. This colour coding will be further used throughout the paper consistently in the presentation of results.

Ultrasonic (US) measurements generally have to be performed on relatively large specimens in order to allow undisturbed wave propagation. Hence, the US tests were performed first on the largest available test specimens, which in our case where the prisms with 300 mm length and 40 mm edge length. Subsequently, cylindrical sub-samples were extracted from these prisms, which were then used for the investigations with X-ray CT and

SIP. Table 1 summarizes the properties of all samples discussed in this paper. Again, it has to be noted that the cylinders are all sub-samples of the corresponding prisms (Figure 3).

**Table 1.** Summary of the SFRC samples used in this study, their geometric properties, fiber dosages and fiber inclinations relatie to the longitudinal sample axis. Cylinders are sub-samples of prisms, as shown in Figure 3.

| Sample | Fiber Dosage [kg/m$^3$] | Length [mm] | Width/Diameter [mm] | Fiber Inclination [deg] |
|---|---|---|---|---|
| Q40—Prism | 40 | 300 | 80 | 90 |
| Q40 ∣∣∣ Prism | 40 | 300 | 80 | 0 |
| Q40 B-40* Cylinder | 40 | 150 | 50 | random |
| Q40—Cylinder | 40 | 150 | 50 | 90 |
| Q40 ∣∣∣ Cylinder | 40 | 150 | 50 | 0 |
| Q0F Cylinder | 0 | 150 | 50 | - |
| Q80 ∣∣∣ Cylinder | 80 | 150 | 50 | 0 |

**Figure 3.** Photograph of the cast prismatic specimens (following being cut halfway along their length) and the extracted cylindrical sub-samples (**left**). The samples discussed in further detail are color-coded. Close-up on a selection of cylindrical sub-samples (**right**).

## *2.2. Methods*

### 2.2.1. X-ray Computed Tomography

The CT examinations were performed using a micro-CT system designed by BAM. The system has a 225 kV microfocus X-ray tube and a flat detector with 2048 × 2048 pixels (Figure 4). From the 2000 projection images, taken during a 360-degree rotation of the sample, a volume data set with 1001 × 1001 × 1981 voxels (i.e., 3D-pixels) is generated in the subsequent image reconstruction. During each CT scan, an entire specimen was imaged, which, given the specimen size, resulted in a resolution (voxel size) of 80 µm. The X-ray CT measurements were collected on all cylindrical specimens presented in Table 1.

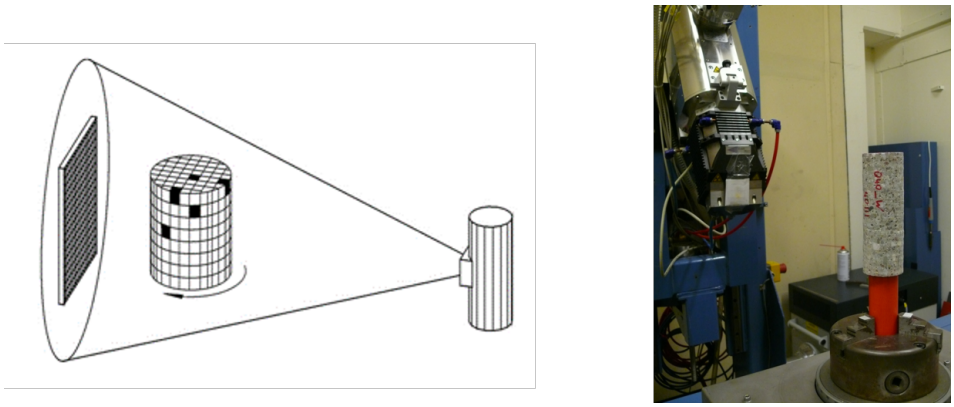

**Figure 4.** Schematic of the X-ray CT measurement principle (**left**) and photograph of the used CT system with SFRC sample placed on the rotating table (**right**).

### 2.2.2. Spectral Induced Polarization

The resistivity measurements or, as typically referred to in geophysics, spectral induced polarization (SIP) measurements were performed using a SIP-ZEL (Zentralinstitut für Elektronik) device [25]. Electrical four-point measurements in Wenner configuration were performed over a frequency range from 1 mHz to 45 kHz. A sample holder similar to the one described in [26] was used, the only difference being that it was larger and could accommodate cylindrical samples of 50 mm diameter and 150 mm length (Figure 5, right). An alternating electrical current was introduced across the outer steel caps and the potential decay across the inner ring wires was recorded. The measured electrical resistivities are complex values and can either be expressed as spectra of amplitude and phase or real and imaginary parts. In the following sections, both amplitude and phase of the resistivity as well as real and imaginary parts of the conductivity of our samples will be presented (Figure 5, left). As the drilling of the cylindrical sub-samples from the originally longer, prismatic samples required water cooling, all samples were dried at 40 °C for 24 h prior to the measurement. For the galvanic coupling between the electrodes and the sample in the SIP sample holder, we used 1.5% agar–agar gel. The SIP data were measured on all cylindrical samples given in Table 1.

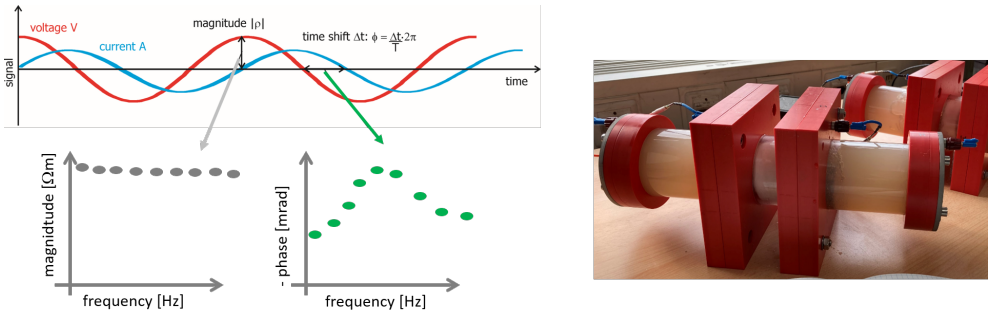


**Figure 5.** SIP signal for a distinct frequency (**top left**). The applied voltage V causes a subsequent current A signal, which is shifted in time. The amplitude ratio of the two signals is the resistivity magnitude $|\rho|$ (in Ωm due to geometrical considerations of sample diameter and length) and their time shift is related to as phase angle Φ (in mrad or °) (**bottom left**). SIP 4-point measurement cell, where the sample is placed in the middle and the electrodes are galvanically coupled with gel (**right**).

### 2.2.3. Ultrasound

An ultrasonic measuring system, consisting of a PC, a rectangular transmitter, a DAQ-Pad (manufactured by NI) for data acquisition and two dry contact probes (manufactured by ACS Group) for generation and reception of ultrasonic transverse waves was used. The ultrasonic transmission pulse is emitted by the transmitter (T), passes through the test body and is received at the receiver (R)s ( see Figure 6). The signal is then digitized using an analogue-to-digital converter (A/D) and transferred to the PC via the USB interface. The probes require no coupling agent and are pressed against the concrete surface of the test specimens by spring force alone. The polarization of the ultrasonic wave in the concrete test specimen can be altered by rotating the probes, as shown schematically for two polarization states in Figure 6 (right). The probes have a centre frequency of $f_M = 50$ kHz and are excited with a bipolar square wave signal of $u_{pp} = 300$ V. The measurements were carried out on all the prismatic specimens shown in Table 1. Each specimen is measured with different angles of polarization (0°, 45°, 90°, 180°, 225° and 270°). In particular, variations in the signal spectra due to changes in the polarization of the ultrasonic waves were studied.

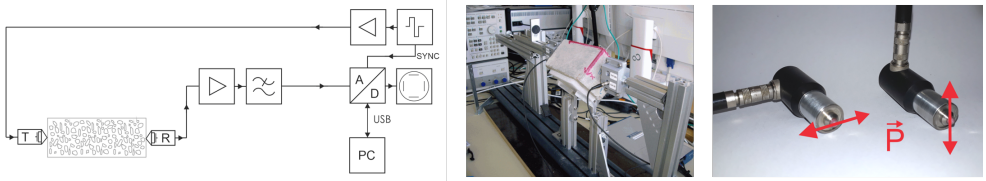


**Figure 6.** Ultrasonic measuring system: block diagram (**left**), photo of the measurement set-up (**centre**) and close-up, of the ultrasonic probes (**right**). In the close-up the polarization $\vec{P}$ of the transmitters is shown in red.

## 3. Results

### *3.1. X-ray Computed Tomography (CT)*

Fiber identification and orientation analysis was completed using the program VGStudioMAX 3.3 (Volume Graphics GmbH). The results of the analysis are presented in terms of spherical coordinates (Figure 7, top left). As the fibers are oriented in all three spatial directions, this representation is the most suitable. In our opinion, a cylindrical coordinate system (using polar coordinates supplemented by a Cartesian coordinate for the height) would have been better to represent the data layer by layer focussing then only on the fiber orientation within one respective cylindrical section in 2D. In this study, though, we aim to analyse all fiber orientations in one sample in 3D.

In the spherical coordinate system we use, orientations are characterized by angles $\Theta$ and $\Phi$. In the Cartesian coordinate system used for these measurements, the cylindrical axis of the sample is denoted as the z-axis. The angle $\Theta$ represents the azimuthal angle in the x-y plane from the x-axis, with $0 < \Theta < 360°$. The angle $\Phi$ represents the polar angle from the positive z-axis, with $0 < \Phi < 180°$.

Figure 7 provides fiber renderings and orientation histograms for all five cylindrical samples shown in Table 1. The orientation histograms are shown in the form of orthographic projections, where the centre of the projection is the z-axis (i.e., the cylindrical axis). Thus, these projections represent, effectively, the portion of the fiber orientation histogram plotted on the upper half of the sphere shown in the upper left of Figure 7. Since the fibers are considered to be symmetric about their lengths, it is assumed that differences between the lower and upper halves of the histogram sphere are negligible, which has also been verified visually during data analysis.

During fiber orientation analysis, the fibers were not individually identified, separated and analysed. Rather, composite orientation information was calculated for all steel fiber material in the specimens. This means that the resulting orientation measurements contain not only orientation data related to the primary axis of the fibers, but also orientation data related to the hooked ends of the fibers. Although this effect introduces a partial distortion of the data, the hook-based effects are considered to be acceptable given the relatively small size of the fiber hooks in comparison to the overall fiber dimensions.

The "Fiber Composite Analysis" module automatically scales the colour coding in the polar colour plot to the deviations found from the orientation with the highest frequency. Since there is no fibre material in sample Q0F, the module scales the colour coding to the orientation values determined on dense aggregates. These aggregate related orientation values are no longer visible in the samples containing fibres with the same parameter setting. Therefore, the colour coding for Q0F was manually adjusted so that the colour scale is comparable with the other polar plot representations. Clear differences in the histogram characteristics can, for instance, be observed between the three samples Q40—, Q40❙❙❙ and Q40* in Figure 7.

### *3.2. Spectral Induced Polarization*

The SIP data collected on all five cylindrical samples listed in Table 1 and the measured real and imaginary electrical conductivities along with the amplitude and phase spectra are plotted in Figure 8. Though all samples were measured in a dry state (meaning that there is no significant pore fluid and electrical conductivity was not possible due to ion

movement), we measured relatively low electrical resistivities between 10 and 800 Ohm*m (Figure 8, left). Most of the samples, besides Q0F which does not contain steel fibers, moreover showed distinct polarization behaviour with absolute phase values well above 20 mrad. As could be expected, the sample Q80 ||| showed, due to its high fiber content, the lowest resistivity magnitude and highest polarizability. These characteristics were less pronounced for the three samples with 40 kg/m$^3$ fiber content. When comparing the results of these latter three samples, Q40|||, where the steel fibers are oriented along the sample axis (and along the electrically induced current flow within the SIP sample holder), features the lowest electrical resistivity amplitude. For the sample Q40*, where the steel fibers are randomly distributed, the electrical resistivity increases and for sample Q40—, where steel fibers are oriented perpendicularly to the induced current flow, we measure the highest resistivity values for a sample containing fibers. Furthermore, from their electrical polarization behavior, these three samples can clearly be differentiated. The sample Q40||| Cylinder is most polarizable, with up to −400 mrad. When the steel fibers are randomly distributed (i.e., Q40* Cylinder), the electrical polarizability decreases to about −350 mrad and when the fibers are perpendicular to the sample axis (and induced electrical field) (i.e., Q40—Cylinder), the polarizability becomes less than −50 mrad.

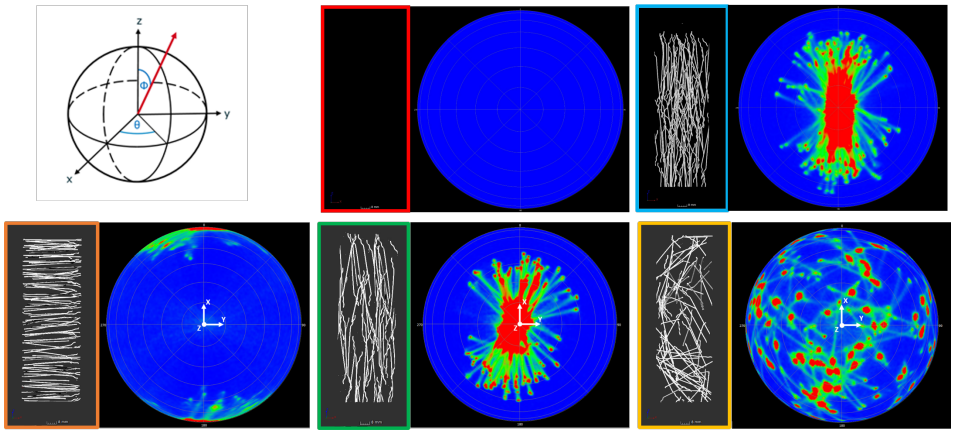


**Figure 7.** Spherical coordinate system , reproduced from Oesch et al. 2018 under the terms of the Creative Commons Attribution 4.0 International License (https://creativecommons.org/licenses/by/4.0/, accessed on 28 November 2021), (**top left**) ). Fiber renderings and orientation histograms for sample Q0F Cylinder (**top centre**), Q80 ||| Cylinder (**top right**), Q40—Cylinder (**bottom left**), Q40 ||| Cylinder (**bottom centre**), Q40* Cylinder (**bottom right**). Histogram radius: $0 < \Phi < 90°$; histogram circumference: $0 < \Theta < 360°$.

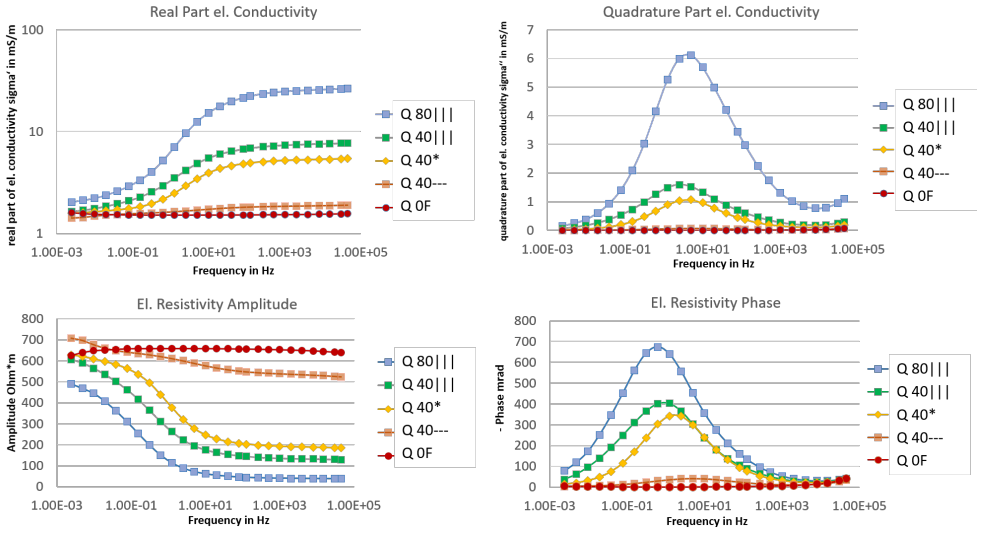


**Figure 8.** Spectral Induced Polarization spectra of steel fiber reinforced concrete samples Q80 ||| Cylinder, Q40 ||| Cylinder, Q40* Cylinder, Q40—Cylinder and Q0F Cylinder. Real and quadrature parts of electrical conductivity (**top**) and resistivity amplitudes and phases (**bottom**).

Given that the concrete mix and the dosage of steel fibers within these three samples was constant, we can assume that the observed differences in the electrical resistivity behavior are due to the fiber orientation. Thus, we can observe, for instance, that the position of the phase peak slightly shifts towards higher frequencies with increasing amount of steel fibers tilted away from the direction of the induced electrical current flow (which coincides with the long axis of the cylindrical samples).

### *3.3. Ultrasound*

The greatest influence on the ultrasonic signals was expected from the specimen where the steel fibres were oriented perpendicular to the sound propagation (specimen Q40—, Figure 9 top). During the first measurement, the polarization of the ultrasonic waves is 0° and the fibre orientation is 90° (Figure 9, top left). The spectrum shows the centre frequency of the probe at about 50 kHz and strong indications at about 42 kHz and 55 kHz. In this figure, |S(f)| denotes the magnitude of the spectral density in arbitrary units (a.u.). Then, the polarization of the ultrasonic waves was rotated by 90° from 0° (i.e., probe polarization 90°, fibre orientation 90°, Figure 9, top right). Thus, the polarization of the ultrasonic waves and the steel fibres are oriented parallel to each other. The magnitude of the spectrum at about 50 kHz is lower and the higher frequency components are more attenuated. In the Q40 ||| test specimen, the steel fibers are oriented in the direction of sound propagation (Figure 9, bottom). By using a rotation of the polarization, changes in the spectrum are also visible, but the influence on the test frequency and on the higher frequency components is lower. While these measurements do suggest that fibre orientation may have an influence on polarization-induced ultrasonic signal variations, the observed correlations have a limited transferability. A more general validation would require a more thorough measurement program.

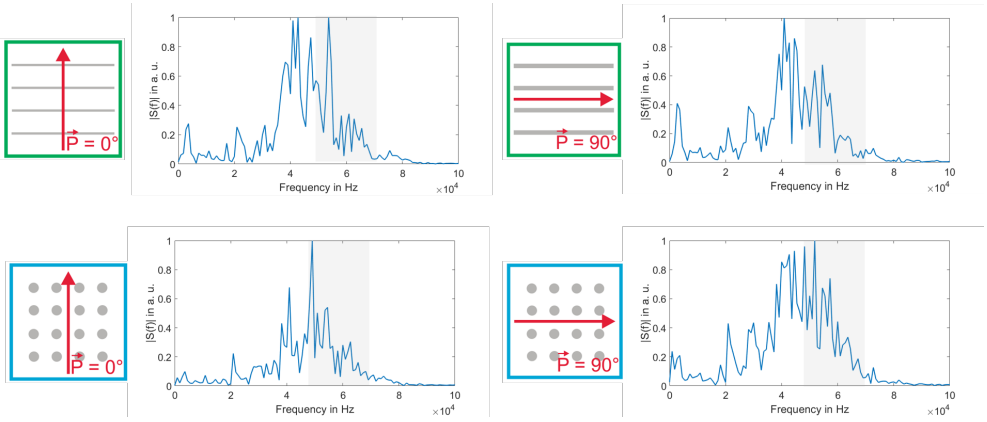


**Figure 9.** Probe polarization and fibre alignment (schematic), spectrum of the corresponding received signals for the samples Q40—Prism (**top**) and Q40 | | | Prism (**bottom**).

## 4. Discussion

The X-ray CT results provide both a qualitative and a quantitative demonstration of the variations in fiber orientation characteristics amongst the specimens. In Figure 7, one can visually observe that nearly all fibers within specimen Q40—Cylinder are well aligned with the x-axis of the sample (i.e., perpendicular to the cylindrical axis). This result is confirmed by the concentrations of fiber orientations measured at ($\Phi$, $\Theta$) = (0°, 90°) and ($\Phi$, $\Theta$) = (180°, 90°), which are the spherical coordinate points corresponding to alignment along the x-axis. Similarly, Figure 7 indicates that the fibers in specimen Q40 | | | Cylinder are well aligned with the z-axis of the specimen (i.e., the cylindrical axis). For specimen Q40* Cylinder, a relatively random scattering of different fiber orientations can be observed (Figure 7). These analysis results, thus, confirm the successfulness of the casting techniques in producing the desired controlled fiber orientation characteristics and can be used as a baseline of fiber orientation information, against which the SIP and ultrasonic measurement results can be evaluated.

In principle, it is conceivable that the measurement results of the non-destructive testing methods are influenced by systematically different (air) pore contents in the specimens due to the manufacturing process and that the observed properties could be distorted as a result. Therefore, the pore radius distributions and the air void contents of the five specimens were determined and compared. Air voids were considered to be those with pore diameters greater than 160 µm, twice the voxel size of the X-ray CT studies performed here. Mercury intrusion porosimetry (MIP) was used as a reference method (compare also [27,28]). For this purpose, 20–30 g of sample material was manually chipped off each of the remnants of the prisms (after the cylinder samples had been taken), dried at 105 °C, and examined by MIP. MIP is used to detect pore sizes down to approximately 3.6 nm. Due to its underlying physics, however, only pore throat diameters can be determined and the volume of wide pore areas (which can only be reached via narrow pore throats) is attributed to the pore throats.

The pore throat diameter distributions are shown in Figure 10, the corresponding total porosities in Table 2. The total porosities of all samples range between 12.14% and 15.19%, but no systematic differences are observed: neither directly between the three samples with 40 kg/m$^3$ fibre content, where the fibres were manually placed in different orientations, nor with respect to the samples with 0 or 80 kg/m$^3$ fibre content. Thus, it can be concluded that the casting process had neither a systematic influence on the overall porosity nor on the pore size distribution of the samples.

The MIP method is not suited, though, for the detection of larger pores, as they are usually accessed via narrow pore throats. However, these might be assessed using X-ray CT. To determine the pore content within the volume examined with CT, a low image grey value threshold for pores is used. The boundary between pore (air) and material (cement) is defined by the determined material surface. The ISO threshold value air/cement,

automatically determined by the software from the histogram analysis, serves as the starting value for the automatic surface detection with local threshold values. In the CT analysis, however, only objects consisting of two or more adjacent voxels are recognized as pores in order to exclude noise ("false pores"). Consequently, only pores with a diameter larger than 160 µm can be detected. The results are shown in Table 2. It is striking that the two samples with longitudinally aligned fibers (Q80 ||| and Q40 |||) show approximately the same and, compared to the other fiber reinforced samples, somewhat lower amount of large pores. This could, however, be due to the better radiolucency of the fibers and the associated reduction of artefacts that are incorrectly recognized as pores by the automatic analysis software. In the sample without fibres, the amount of large pores is only slightly lower. The results may, therefore, be not very reliable due to the interference caused by the steel fibres. Strictly speaking, the pore content can only be reliably compared if the fibre orientation is the same. Thus, it is not possible to deduce the effect of the casting process on the volume of large pores using the measurement data listed here. However, given that the total porosities measured using MIP did not vary strongly in relation to fiber distribution or orientation characteristics, it appears unlikely that porosity variations had a major influence on the results of the SIP and US investigations.

**Table 2.** Porosities determined by X-ray CT and MIP in vol.% and BET surface area in $m^2/g$.

| Sample | X-ray CT-Por. ≥ 160 µm | MIP-Por. ≥ 160 µm | MIP-Por. ≥ 3.6 nm | BET Surface Area |
|---|---|---|---|---|
| Q 80 ||| | 1.9 | 0.6 | 12.22 | 3.89 |
| Q 40 ||| | 1.8 | 0.5 | 15.19 | 5.05 |
| Q 40* | 3.6 | 0.4 | 13.25 | 4.43 |
| Q 40— | 3.4 | 0.8 | 12.14 | 3.44 |
| Q 0F | 1.5 | 0.6 | 12.98 | 4.20 |

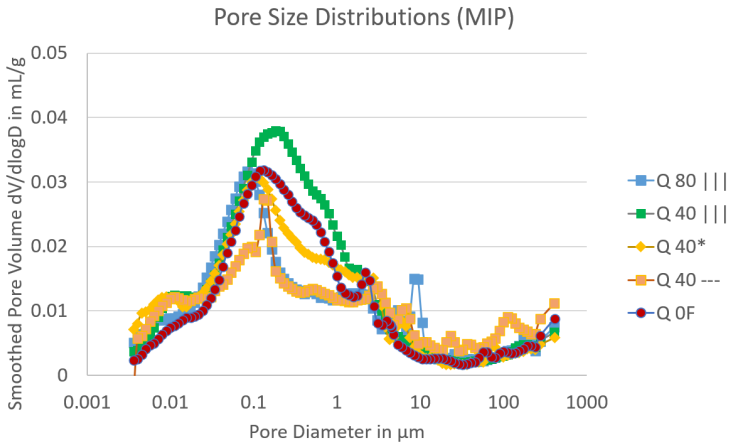


**Figure 10.** Pore throat size distributions of all five samples determined with MIP.

The SIP measurements showed that our results support the findings of [16], which showed that the main orientation of steel fibers in test specimens coincided with the direction of the lowest resistivity. In the present study, we measured, however, not only the resistivity, which has previously been evaluated by [16], but also the frequency dependency of the complex resistivity by evaluating the polarization behavior of our samples. Our data indicate that the phase spectra might be an even more sensitive quantity for measuring fiber orientation than the amplitude spectra as the differences between samples with parallel and perpendicular oriented steel fibers were even more pronounced. The works of [17,18] both focus on the influence of fiber dosage (not their orientation) on the electrical resistivity for samples prepared with random fiber distributions. The fibre dosage of our samples (for instance, 0.5 vol% for Q40—, Q40||| and Q40*) is at the lower end of what the other

working groups used and it is conceivable that by evaluating both resistivity amplitude and phase, we could extract information about fibre orientation and content at the same time.

The observed changes in the ultrasound signal are not very strong and experience has shown that this can also be caused by changes in the coupling. The test specimens are relatively small compared to the ultrasonic wavelength. Due to reflections of the ultrasonic waves at the sides of the test specimen and the superposition of different wave modes, the results are not clear. Thus, further ultrasonic measurements on larger specimens are necessary to confirm these initial promising results. The measurement of steel fiber content and/or orientation with ultrasonic dry contact probes would have the advantage that the concrete surface does not have to be prepared for a measurement. Other influencing variables like the grading curve, the pore structure, cracks or variations in the moisture content of the samples were not regarded in this study. All these parameters can significantly influence the results and sensitivity of SIP or US measurements. Therefore, further research is needed.

## 5. Conclusions

SFRC is still a relatively new building material, which holds great potential for innovative use and design approaches for future concrete structures. The assessment of SFRC properties, such as fiber orientation and dosage, is still difficult, often requiring coring and elaborate lab analysis. Our study focusses on the effectiveness of alternative methods to extract this information non-destructively.

Evaluating the electrical behavior of SFRC samples, we found that both the resistivity magnitude and phase (i.e., the material's capability to polarize) are sensitive to the main fiber orientation. It is conceivable that when both are measured, fiber orientation and content can be assessed. Likewise, for the measured samples we saw that the transmission amplitude of ultrasonic shear waves is slightly diminished and that higher frequency components are attenuated when the polarization of the wave is parallel to the fibers' direction. However, the dimensions of the test specimens have the same order of magnitude as the ultrasound wavelength itself. This results in reflections of the ultrasonic waves from the test body sides and a superposition of different wave modes in the received signal, making the interpretation of the results difficult. In addition, variations in probe coupling have an influence on the received signals. For this reason, further ultrasonic measurements are necessary, using a larger number of test specimens with bigger dimensions, to further investigate these first indications of an influence of the fibres on the ultrasonic signals.

The X-ray CT analysis provided quantitative measurements of fiber orientation as well as visualizations of actual fiber distributions within the specimens. These measurements not only verified the successfulness of the specimen casting technique in producing specimens with controlled fiber orientations. They also can serve as a quantitative basis for assessing correlations between ultrasonic or SIP measurements and actual fiber conditions. An analysis of the statistical correlation between the quantitative fiber orientation data measured using X-ray CT and the phase variations measured using SIP could yield useful mathematical relationships that could be utilized as a basis for expanding fiber orientation assessment using SIP to further applications (such as measurement of larger components or of different fiber types). Such a statistical analysis is the planned topic of the authors' future work in this area.

**Author Contributions:** Conceptualization, S.K., T.O. and P.S.; methodology, all; validation, T.O., D.M., F.M. and S.K.; investigation, T.O., D.M., F.M. and S.K.; resources, P.S.; data curation, T.O., D.M., F.M. and S.K.; writing—original draft preparation, all; writing—review and editing, all; visualization, all; supervision, S.K., T.O. and P.S.; project administration, all. All authors have read and agreed to the published version of the manuscript.

**Funding:** This research received no external funding.

**Acknowledgments:** The authors express their gratitude to company SV Bekaert SA for the provision of steel fibers as material used in this investigation, and the valuable scientific feedback. Moreover, we thank Heiko Stolpe and Marco Lange from BAM for technical support and sample preparation. The opinions expressed in this publication are those of the authors and they do not purport to reflect opinions or views of the supporting organisations.

**Conflicts of Interest:** The authors declare no conflict of interest.

## References

1. Boshoff, W.P.; Altmann, F.; Adendorff, C.J.; Mechtcherine, V. *A New Approach for Modelling the Ingress of Deleterious Materials in Cracked Strain Hardening Cement-Based Composites*; Springer Science and Business Media LLC: Berlin, Germany, 2015; Volume 49, Chapter A, pp. 2285–2295.
2. di Prisco, M.; Colombo, M.; Dozio, D. Fiber-reinforced concrete infibModel Code 2010: principles, models and test validation. *Struct. Concr.* **2013**, *14*, 342–361. [CrossRef]
3. Matthews, S.; van Vliet, A.B.; Walraven, J.; Mancini, G.; Dieteren, G. fib Model Code 2020: Towards a general code for both new and existing concrete structures. *Struct. Concr.* **2018**, *19*, 969–979. [CrossRef]
4. Mark, P.; Oettel, V.; Look, K.; Empelmann, M. Neuauflage DAfStb-Richtlinie Stahlfaserbeton. *Beton- Stahlbetonbau* **2020**, *116*, 19–25. [CrossRef]
5. ACI Committee 544 4R. *Guide to Design with Fiber-Reinforced Concrete*; Technical Report; American Concrete Institute: Farmington Hills, MI, USA, 2018.
6. Goodchild, C. *Eurocodes Recision—An Update*; Technical Report; The Concrete Centre: London, UK, 2016.
7. Holschemacher, K.; Dehn, F.; Müller, T.; Lobisch, F. *Grundlagen des Faserbetons*; Wiley: Hoboken, NJ, USA, 2016.
8. Ferrara, L.; Park, Y.D.; Shah, S.P. Correlation among Fresh State Behavior, Fiber Dispersion, and Toughness Properties of SFRCs. *J. Mater. Civ. Eng.* **2008**, *20*, 493–501. [CrossRef]
9. Gröger, J.; Nehls, N.; Silbereisen, R.; Tue, N.V. Einfluss der Einbau- und der Betontechnologie auf die Faserverteilung und -orientierung in Wänden aus Stahlfaserbeton. *Beton- Stahlbetonbau* **2011**, *106*, 45–49. [CrossRef]
10. Pujadas, P.; Blanco, A.; Cavalaro, S.H.P.; de la Fuente, A.; Aguado, A. Multidirectional double punch test to assess the post-cracking behavior and fiber orientation of FRC. *Constr. Build. Mater.* **2014**, *58*, 214–224. [CrossRef]
11. Lusis, V.; Krasinovs, A.; Konovova, O.; Lapsa, V.A.; Stonys, R.; Macanovskis, A.; Lukasenoks, A. Effect of Short Fibers Orientation on Mechanical Properties of Composite Material–Fiber Reinforced Concrete. *J. Civ. Eng. Manag.* **2017**, *23*, 1091–1099. [CrossRef]
12. Villar, V.P.; Medina, N.F. Alignment of hooked-end fibers in matrices with similar rheological behavior to cementitious composites through homogeneous magnetic fields. *Constr. Build. Mater.* **2018**, *163*, 256–266. [CrossRef]
13. Ledderose, L.; Lehmberg, S.; Budelmann, H.; Kloft, H. Robotergestützte, magnetische Ausrichtung von Mikro-Stahldrahtfasern in dünnwandigen UHPFRC-Bauteilen. *Beton- Stahlbetonbau* **2019**, *114*, 33–42 [CrossRef]
14. Heek, P.; Look, K.; Oettel, V.; Mark, P. Bemessung von Stahlfaserbeton und stahlfaserbewehrtem Stahlbeton. *Beton- Stahlbetonbau* **2021**, *116*, 2–12. [CrossRef]
15. Wichmann, H.J.; Holst, A.; Budelmann, H. Ein praxisgerechtes Messverfahren zur Bestimmung der Fasermenge und - orientierung im Stahlfaserbeton. *Beton- Stahlbetonbau* **2013**, *108*, 822–834. [CrossRef]
16. Lataste, J.F.; Behloul, M.; Breysse, D. Characterisation of fibers distribution in a steel fiber reinforced concrete with electrical resistivity measurements. *NDT E Int.* **2008**, *41*, 638–647. [CrossRef]
17. Solgaard, A.O.S.; Geiker, M.; Edvardsen, C.; Küter, A. Observations on the electrical resistivity of steel fiber reinforced concrete. *Mater. Struct.* **2013**, *47*, 335–350. [CrossRef]
18. Fiala, L.; Toman, J.; Vodička, J.; Ráček, V. Experimental Study on Electrical Properties of Steel-fiber Reinforced Concrete. *Procedia Eng.* **2016**, *151*, 241–248. [CrossRef]
19. Gebretsadik, B. Ultrasonic Pulse Velocity Investigation of Steel Fiber Reinforced Self-Compacted Concrete. Master's Thesis, University of Nevada, Reno, NV, USA, 2013.
20. Wiggenhauser, H.; Niederleithinger, E.; Milmann, B. Zerstörungsfreie Ultraschallprüfung dicker und hochbewehrter Betonbauteile. *Bautechnik* **2017**, *94*, 682–688. [CrossRef]
21. Liu, J.; Li, C.; Liu, J.; Cui, G.; Yang, Z. Study on 3D spatial distribution of steel fibers in fiber reinforced cementitious composites through micro-CT technique. *Constr. Build. Mater.* **2013**, *48*, 656–661. [CrossRef]
22. Herrmann, H.; Pastorelli, E.; Kallonen, A.; Suuronen, J.P. Methods for fiber orientation analysis of X-ray tomography images of steel fiber reinforced concrete (SFRC). *J. Mater. Sci.* **2016**, *51*, 3772–3783. [CrossRef]
23. Oesch, T.; Landis, E.; Kuchma, D. A methodology for quantifying the impact of casting procedure on anisotropy in fiber-reinforced concrete using X-ray CT. *Mater. Struct.* **2018**, *51*, 1–13. [CrossRef]
24. N.V. Bekaert S.A. EC Declaration of Performance Dramix® 5D 65/60BG (Creation Date 2019/07/10). Technical Report. 2019. Available online: https://www.bekaert.com/en/product-catalog/content/dop/dramix-5d-technical-documents (accessed on 28 November 2021).
25. Zimmermann, E.; Kemna, A.; Berwix, J.; Glaas, W.; Münch, H.M.; Huisman, J.A. A high-accuracy impedance spectrometer for measuring sediments with low polarizability. *Meas. Sci. Technol.* **2008**, *19*, 105603. [CrossRef]

26. Kruschwitz, S. Assessment of the Complex Resistivity Behavior of Salt Affected Building Materials. Ph.D. Thesis, Bundesanstalt für Materialforschung und -prüfung (BAM), Berlin, Germany, 2008.
27. Kruschwitz, S.; Halisch, M.; Dlugosch, R.; Prinz, C. Toward a better understanding of low-frequency electrical relaxation—An enhanced pore space characterization. *Geophysics* **2020**, *85*, MR257–MR270. [CrossRef]
28. Washburn, E.W. The Dynamics of Capillary Flow. *Phys. Rev.* **1921**, *17*, 273–283. [CrossRef]